



Karthikeyan, V. , Oo, S. L., Surjadi, J. U., Li, X., Theja, V. C.S., Kannan, V., Lau, S. C., Lu, Y., Lam, K.-H. and Roy, V. A.L. (2021) Defect engineering boosted ultrahigh thermoelectric power conversion efficiency in polycrystalline SnSe. *ACS Applied Materials and Interfaces*, 13(49), pp. 58701-58711. (doi: [10.1021/acsami.1c18194](https://doi.org/10.1021/acsami.1c18194))

The material cannot be used for any other purpose without further permission of the publisher and is for private use only.

There may be differences between this version and the published version. You are advised to consult the publisher's version if you wish to cite from it.

<https://eprints.gla.ac.uk/259938/>

Deposited on 02 December 2021

Enlighten – Research publications by members of the University of
Glasgow

<http://eprints.gla.ac.uk>

Defect Engineering Boosted Ultrahigh Thermoelectric Power Conversion Efficiency in Polycrystalline SnSe

Vaithinathan Karthikeyan^a, Saw Lin Oo^a, James Utama Surjadi^b, Xiaocui Li^b, Vaskuri C. S. Theja^a, Venkataramanan Kannan^c, Siu Chuen Lau^e, Yang Lu^b, Kwok-Ho Lam^d, Vellaisamy A. L. Roy^{e}*

^a Department of Materials Science & Engineering, City University of Hong Kong, Kowloon Tong, Hong Kong

^b Department of Mechanical Engineering, City University of Hong Kong, Kowloon Tong, Hong Kong

^c Department of Physics, SCSVMV University, Kanchipuram, India.

^d Department of Electrical Engineering, The Hong Kong Polytechnic University, Hung Hom, Hong Kong

^e James Watt School of Engineering, University of Glasgow, Glasgow G12 8QQ, United Kingdom

Corresponding author:

Email id: roy.vellaisamy@glasgow.ac.uk

Abstract

2D layered atomic arrangement with ultralow lattice thermal conductivity and ultrahigh figure of merit in single-crystalline SnSe drew significant attention among all thermoelectric materials. However, the processing of polycrystalline SnSe with equivalent thermoelectric performance as single crystal SnSe will have a great technological significance. Herein, we demonstrate a high zT of 2.4 at 800 K through optimization of intrinsic defects in polycrystalline SnSe via controlled alpha irradiation. Through a detailed theoretical calculation of defect formation energies and lattice dynamic phonon dispersion studies, we demonstrate that the presence of intrinsically charged Sn vacancies can enhance the power factor and distort the lattice thermal conductivity by phonon-defect scattering. Supporting our theoretical calculations, the experimental enhancement in the electrical conductivity leads to a massive power factor of 0.9 mW/mK^2 and an ultralow lattice thermal conductivity of 0.22 W/mK through vacancy-phonon scattering effect in polycrystalline SnSe. The strategy of intrinsic defect engineering of polycrystalline thermoelectric material can increase the practical implementation of low-cost and high performing thermoelectric generators.

Keywords: *Defect Engineering, Alpha Irradiation, Phonon Scattering, Lattice thermal conductivity, Thermoelectrics*

1. Introduction

Thermoelectric materials stand as the major scope for direct conversion of heat energy to electricity because of their emission-free, vibration-free operation and eco-friendly nature. The power conversion efficiency of this system is controlled by the interrelationship in their figure of merit (zT) expressed as $zT = (S^2\sigma/\kappa) T$, where S , σ , κ and T are Seebeck coefficient, electrical conductivity, thermal conductivity and absolute temperature, respectively¹⁻⁵. To breakdown, their complex interrelationship, several strategies like band structure engineering⁶⁻⁸, band convergence⁹⁻¹¹, inducing resonant levels¹²⁻¹⁴, energy barrier filtering¹⁵⁻¹⁷, nano-structuring¹⁸⁻²⁰, lattice anharmonicity²¹⁻²³, Rashba effect²⁴ and hierarchical architectures^{25,26} are introduced. Most of these strategies ended up only improving the power factor of the thermoelectric material. Approaches to enhance the zT can be categorized into power factor boosting and thermal conductivity reduction; practically, enhancing the thermopower will add to the electronic part of thermal conductivity(κ_e). Whereas the lattice ordering determines the lattice thermal conductivity, it is the only independent parameter in the figure of merit (zT). Thus creating anharmonicity in the crystal lattice will effectively serve as an efficient scattering source for phonon transportation without hindering the carrier transport^{27,28}. In this aspect, defect engineering in thermoelectric materials is gaining more attention due to their ability to simultaneously tune the intrinsic carrier density and phonon transport properties. Inducing defect levels into the material can create a strong lattice anharmonicity and systematically decrease the lattice thermal conductivity. Tin selenide (SnSe) is a well-known p-type semiconductor with a bandgap of 0.86eV and a large resistivity between 10^1 - $10^5 \Omega \text{ cm}$ at room temperature²⁹⁻³¹. In addition, SnSe possesses an ultra-low lattice thermal conductivity of $< 0.4 \text{ W/mK}$ at 923 K. SnSe resembles a distorted NaCl crystal structure with a simple orthorhombic layered arrangement. The hierarchical layered arrangement of SnSe exhibits different characteristic electrical and thermal properties along with its a , b and c axial directions. The source of low thermal conductivity arises from the large Gruneisen parameter causing strong anharmonicity^{21,23}. Anharmonicity is experienced due to the weak Sn-Se bonding explained by Heremans²² using a simple ball-spring model. The origin of the p-type in SnSe was confirmed from the intrinsic defect formation and its transition energy levels³². Improvements over the thermoelectric performance and the science behind the ultra-low thermal properties had been reported^{33,34}. However, the detailed analysis of the physics behind defects induced thermal and

electrical properties are still being explored. Recently, polycrystalline SnSe with the highest zT of ~ 2.5 , equivalent to the single crystalline SnSe performance via dopant and surface SnO_2 removal, was reported. Surface oxide removal treatment and hole doping simultaneously enhanced its electrical conductivity³⁵. Moreover, this approach of hole doping in the solid solution efficiently suppresses phonon transportation and thus the lattice thermal conductivity³⁶. These studies prove that polycrystalline SnSe conceals many thermoelectric properties to be explored. On the other hand, defect engineering is demonstrated to improve zT and lattice defects could easily be introduced by ionizing radiation. In comparison with the doping process, defect engineering in materials via ionizing radiation is an effective way for improving the performance of different families in thermoelectric materials^{37–39}.

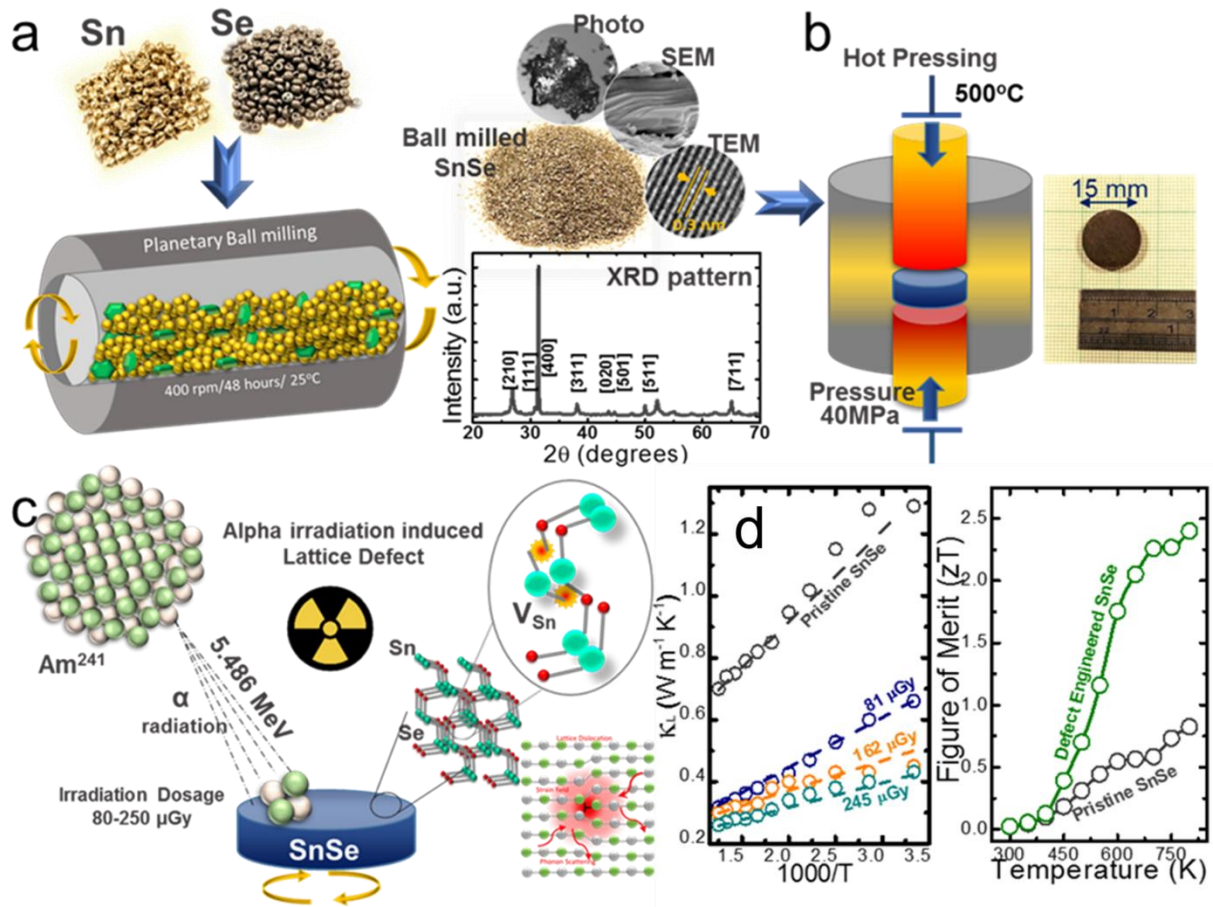


Figure 1 Schematic illustration of the (a) ball-milled synthesis of SnSe (b) hot-press fabrication process (c) Mechanism of the alpha particle induced lattice defect in SnSe (d) Dominance of phonon scattering induced by strain field and lattice dislocations and simultaneous enhancement in figure of merit.

Here, we report on systematic theoretical and experimental analysis of intrinsic defect induced thermoelectric properties of polycrystalline SnSe. Intrinsic defects are generated in the SnSe material's lattice through controlled exposure of alpha irradiation source. The alpha radiation induces random vacancy defects in the material, which acts as intrinsic dopants leading to ultralow thermal properties. Additional bands in its phonon density of states and formation of gap states in the electronic density of states have been achieved. The induced defects support the increase in power factor with a parallel rise in Seebeck and electrical conductivity. The anharmonicity caused by irradiation-induced defects is studied by Terahertz Time-domain spectroscopy (THz-TDS) which agrees well with our argument on the decrease in the total thermal conductivity. As a result, for the first time, we report a high zT of 2.4 and an ultra-low total thermal conductivity of 0.22 W/m K at 823 K due to the synergistic phonon scattering by the irradiation-induced defect density in polycrystalline SnSe. Anisotropy dependent thermoelectric properties are presented in the supporting information.

2. Experimental Methods

Tin (Sn, 99.99%) and Selenium (Se, 99.99%) powders are weighed to a stoichiometric ratio of 1:1 and loaded into a stainless steel ball milling jar mechanical alloying at 400 rpm for 48 hours. The resultant powdered SnSe microflakes were used for pelleting by hot-pressing in a graphite mould under vacuum at 500°C with a heating rate of 30°C/min at 50MPa pressure for 30 minutes to form a pellet with a density of 5.97 g/cm³. The hot-pressed samples were then exposed to alpha particle irradiation with 5.486 MeV at different dose rates of 81 μGy (30 mins), 162 μGy (45 mins) and 245 μGy (60 mins) by Am²⁴¹ isotope under a controlled environment as illustrated in Figure 1. TRIM Simulation for the analysis of alpha particles penetration depth in the SnSe samples were performed as shown in supplementary data S1. The powder X-ray diffraction pattern for each sample was measured using Bruker D2 diffractometer with Cu Kα ($\lambda = 1.54 \text{ \AA}$). Raman properties were measured using a Renishaw InVia confocal Raman spectrometry with a 633 nm laser source. Transport properties, hall carrier concentration were measured using the Lakeshore Hall measurement system in the magnetic field range -2T and +2T at different temperature ranges. Field Emission Scanning Electron Microscopy (FE-SEM) FEI Quanta 200FEG was used to analyze the layered internal alignment of the hot-pressed samples. Terahertz Time-Domain Reflectance Spectroscopy (THz-TDS) was measured using TeraSys AIO spectrometer for analyzing the

anharmonicity caused by the defect concentration. Detailed X-ray Photoelectron Spectroscopy (XPS) studies were conducted using VG ESCALAB 220i-XL for High-resolution scanning of Sn and Se elements. Thermoelectric properties characterization of the samples for Seebeck coefficient (S) and electrical conductivity (σ) were performed using Netzsch SBA 458 Nemesis through standard four-probe direct current measurement method under argon atmosphere between 300-800 K. Thermal conductivity (κ) was determined through the relation $\kappa = \alpha C_p \rho$, where α and C_p are the thermal diffusivity and specific heat of the sample measured through light flash method using Netzsch LFA 467 hyperflash and the density (ρ) was measured through Archimedes' method. Thermoelectric properties reported are measure in the direction perpendicular to the plane.

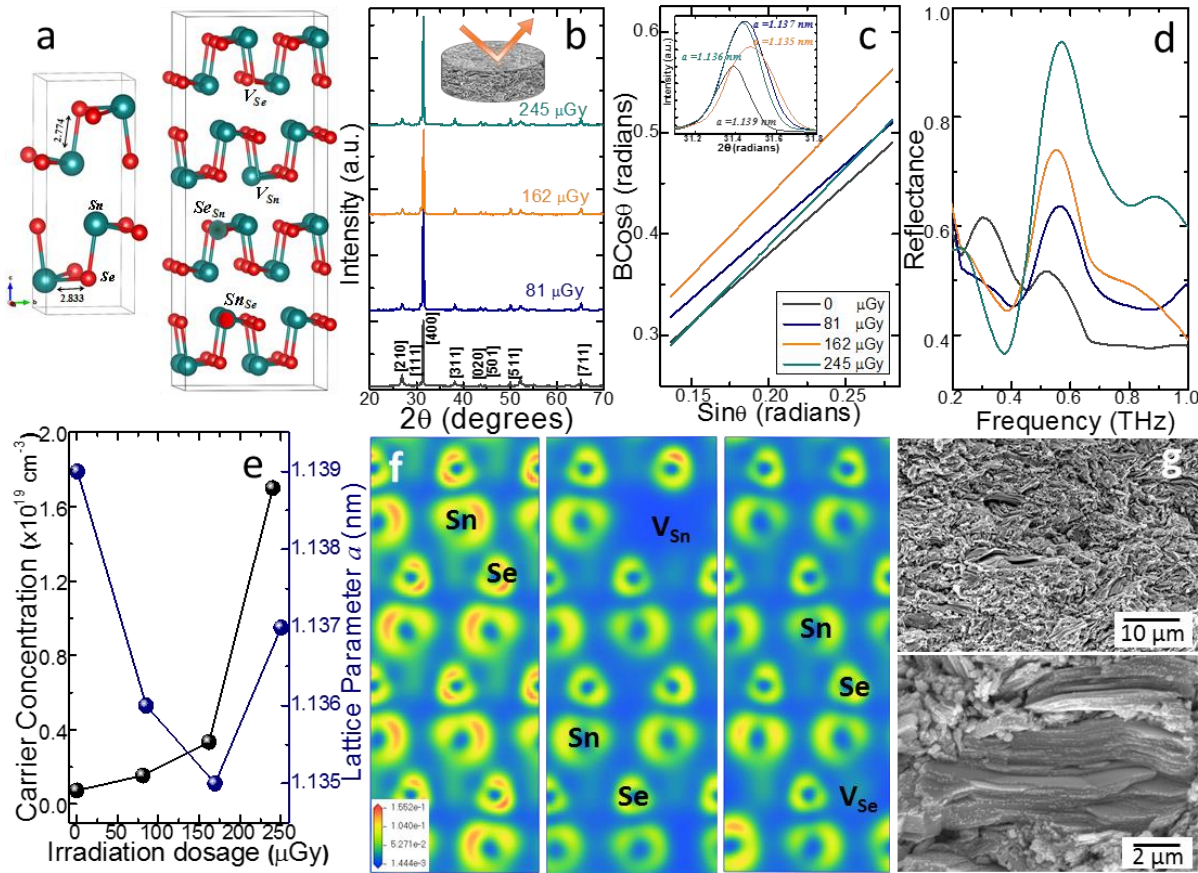


Figure 2 (a) Crystal structure of layered SnSe and illustration of defective SnSe structure (b) Powder XRD pattern of the polycrystalline SnSe measure under different radiation dosage (c) Williamson-Hall plot analysis indicating the microstrain induced on the crystal lattice (d) shows the resonance peak of THz-TDS indicating the lattice anharmonicity induced by the intrinsic defects generated (e) Relationship between the decrease in lattice parameter and increasing carrier density to irradiation dosage in SnSe samples (f) Electronic charge density of SnSe in the presence of point defects (g) cross-sectional FE-SEM image of hot-pressed SnSe sample exhibiting layered structure.

Theoretical calculations of the electronic density of states for pristine SnSe and defect induced SnSe were performed using Density Functional Theory calculations using Vienna Ab Initio Simulation Package (VASP). GGA+U approach proposed by Dudarev et al. was used to improve the total electronic band structure⁴⁰. Geometrical optimization and relaxation of the structure were performed with a conjugated gradient algorithm before evaluating the electronic density of states. The reciprocal space was sampled with 6 x 6 x 6 Monkhorst-Pack k-point grid, and 500 eV energy cutoff was used for the plane-wave basis set. The Sn and Se vacancy defects were introduced into a 3 x 3 x 3 supercell for analyzing the influence of the defects in the crystal structure. Lattice dynamics calculations for phonon dispersion, phonon density of states and electronic charge density plot for the system with Sn and Se vacancy defects were calculated using CASTEP module in Materials Studio 8.0.

3. Results and Discussions

As illustrated in Figure 2a, SnSe possesses a double-layered geometrical arrangement of Sn and Se atoms interconnected in a zig-zag pattern lying in the same axis plane. Their corresponding bond lengths are calculated as 2.774 Å and 2.833 Å with experimental lattice parameters values $a=11.39$ Å, $b=4.21$ Å, $c=4.45$ Å³¹. Powder X-ray diffraction pattern of the ball-milled and hot-pressed samples indexed in figure 2b presents the orthorhombic structure of SnSe polycrystals. XRD pattern of the α - irradiation-exposed samples clearly shows the right-shifted [400] peak with an increase in dose rate of 81 μ Gy, 162 μ Gy and 245 μ Gy, respectively. This shift in 2θ corresponds to the decrease in the lattice parameter (a) as a result of the increasing vacancy defect concentration in the lattice with respect to the irradiation exposed dose rates³⁸. The lattice strain induced by the ionizing α - radiation dosage was calculated by the Williamson-Hall method⁴¹ as shown in figure 2c, where the amount of strain induced in the lattice after α - irradiation explains the possibility of generating charged Sn vacancy defects. The W-H plot was calculated using [400], [311], [020], [501] and [511] XRD peak positions and their FWHM, where the slope and intercept indicate the strain-induced and the grain size, respectively. Comparison of the increase in hole concentration to the lattice parameter with respect to the irradiation dose is shown in figure 2e. This comparison supports the claims of irradiation dosage inducing charged Sn vacancy defects, which is in good agreement with Vegard's law⁴².

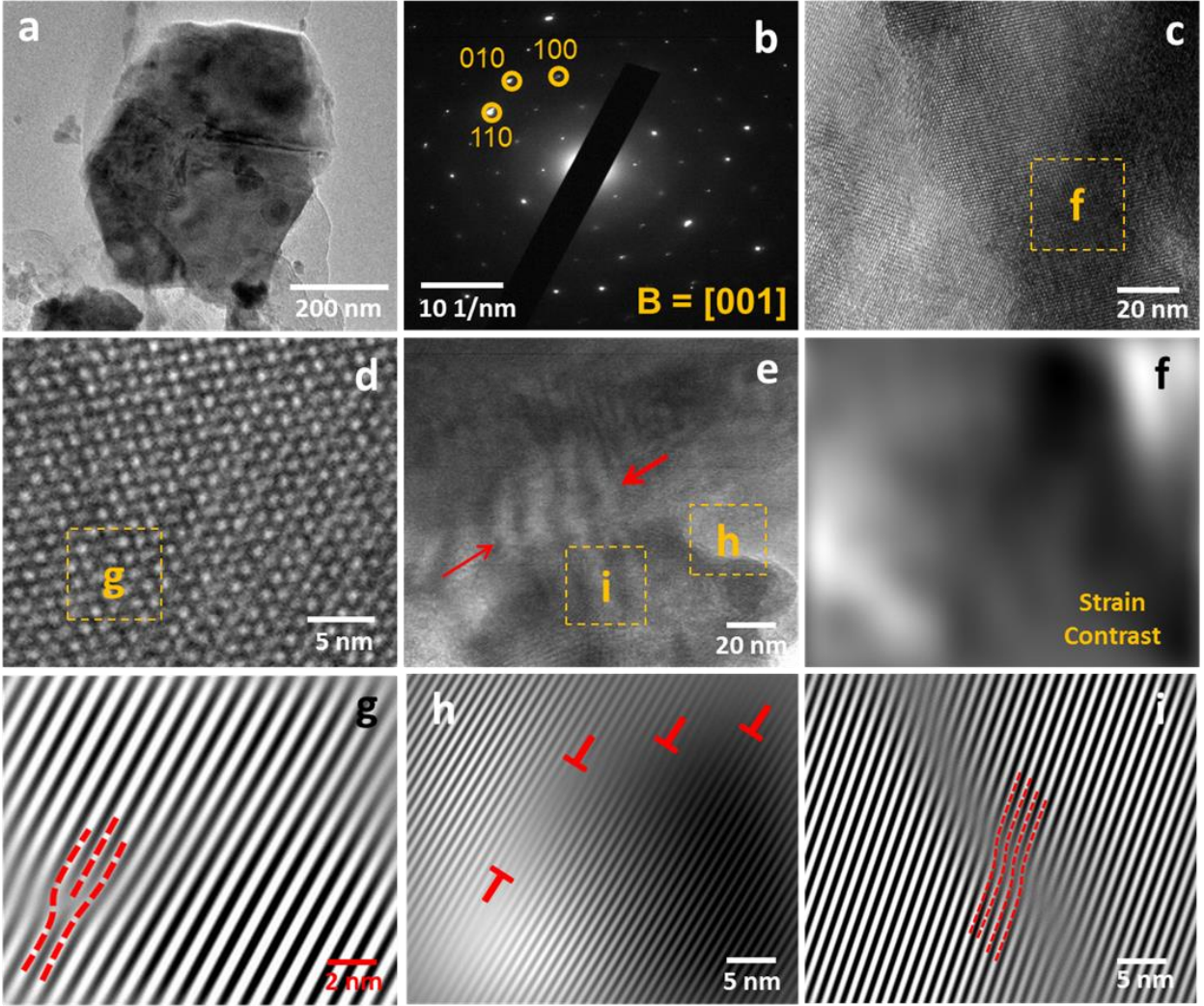


Figure 3 (a) TEM image of the alpha particle irradiated SnSe flakes with dosage of $245\mu\text{Gy}$ (b) SAED pattern of the SnSe flake (c) HRTEM image exhibiting the edge dislocation region (d) High-resolution image of the SnSe flake representing the atomic positions (e) demonstrates the strain induced in the SnSe lattice (f) shows the strain contrast (g), (h) and (i) exhibits the inverse FFT of the lattice dislocations and the strain defects incurred by the irradiation.

Additionally, for experimental characterization of the phonon-defect scattering induced in the material, we measured the time-domain terahertz reflection spectrum (THz-TDS), as shown in figure 2d. Terahertz spectroscopy analysis reveals the lattice and carrier dynamics of semiconductor materials, especially for materials with electron-phonon solid coupling where carrier-lattice interaction produces localized lattice distortions^{43,44}. These lattice distortions in the material can be analyzed via the THz reflectance spectrum, which induces anharmonic frequencies, as shown in figure 2d. The presence of intrinsic defects increases with radiation dosage, evident from the THz reflectance as the resonant intensity increases between 0.4 – 0.8

THz. FE-SEM imaging of the hot-pressed pellet's cross-section shows a perfect layered alignment pattern that supports good electrical conductivity in the samples. Interpretation for the existing correlation between lattice parameter and the hall carrier concentration is the orbital bonding that produces peripatetic carriers. However, in SnSe the formation of vacancy defects in the crystal lattice leads to an increase in hole concentration¹³. These Sn vacancies and their migration tend to accelerate the dislocation density as recorded in many other ionic crystals.

For a deep understanding of the irradiation-induced defect in the crystal lattice TEM studies were performed and maximum irradiation of 245 μGy was used for the measurement. Figure 3a shows the TEM image of SnSe plate with strain and dislocations. The following SAED pattern shows the orthorhombic structure with the presence of [001] plane⁴⁵. The corresponding high-resolution TEM image in figure 3c shows the thickness contrast and edge dislocation, whereas figure 3f shows the strain contrast of the selected area of the SnSe plate. The strain contrast demonstrates the lattice strain induced in the material by the alpha irradiation. Figure 3d shows the magnified HRTEM of the lattice arrangement in the SnSe plate. Dense dislocation and lattice strain are present all over the SnSe plates shown in figure 3e, with arrow marks representing the highly strained lattice distortion. Figure 3g-3i shows the inverse fast Fourier transform of the HRTEM exhibiting the high density of dislocation and lattice bending/distortion. TEM comparison for the pristine SnSe samples is provided in the Supplementary information S2.

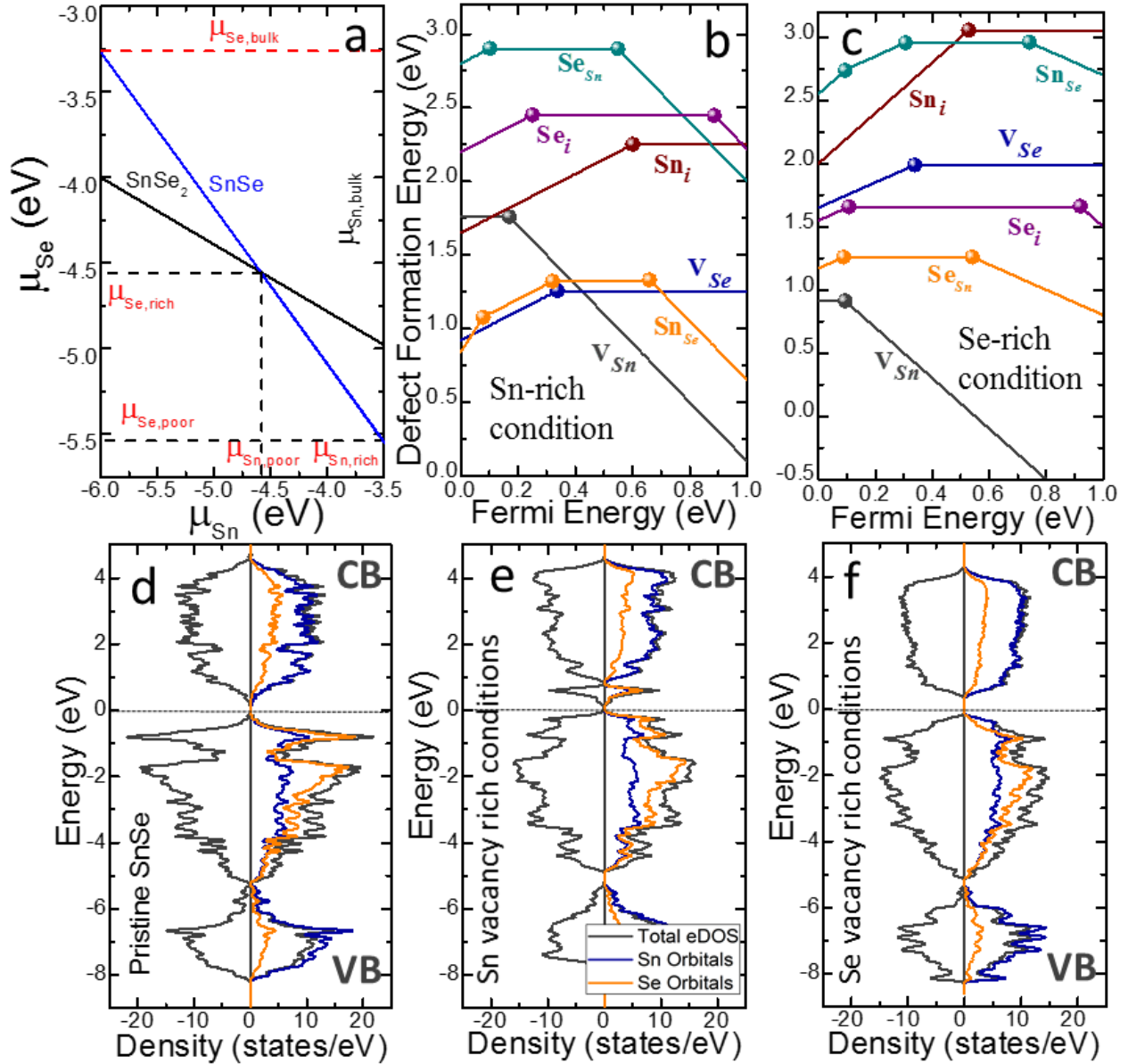


Figure 4 (a) Thermodynamic growth conditions of SnSe crystal where the horizontal and vertical lines indicate the higher chemical potential limits of Sn and Se determined from the native phase of Sn and Se respectively (b), (c) Calculated defect formation energies of intrinsic defect in SnSe under Sn-rich and Se-rich conditions (d), (e) and (f) Compares of the calculated electronic density of states of SnSe under Sn vacancy rich and Se vacancy rich condition exhibiting defect-related changes.

Hence, for a deep analysis of the intrinsic defect in SnSe, VASP calculation on the electronic density of states under Sn vacancy (V_{Sn}) and Se vacancy (V_{Se}) rich conditions were performed as shown in figure 4d, which matches well with our experimental claims on the presence of positively charged Sn vacancy defects⁴⁶⁻⁴⁸. Figure 4d explains the theoretical calculation of electronic density of states of pristine SnSe (i.e. $\text{Sn}_{16}\text{Se}_{16}$), Sn vacancy rich conditions ($\text{Sn}_{14}\text{Se}_{16}$) and Se

vacancy rich conditions (Sn₁₆Se₁₄). Calculation of the pristine SnSe electronic structure shows a bandgap of 0.45 eV at PBE level, which is smaller than the experimental band gap of 0.8 eV. It can be seen that the lower energy valence bands limit ranges from -5.5 eV to -2 eV, which is attributed to the interaction between the Sn 5p orbital and Se 4p orbital states. In contrast, the upper valence band states result from the interaction between Sn 5s orbitals with Se 4p orbital states. The conduction band is formed from the interaction of Sn 5p and Se 4p orbital states⁴⁶. The presence of defects in a system introduces an additional level in the band structure near the Fermi level; similarly, under V_{Sn} rich condition (Sn poor condition, figure 4e), the bandgap shows an apparent decrease to 0.25 eV with the formation of a gap state between the valence and conduction band edge which is due to the interaction of Sn 5p and Se 4p orbital states. As seen from the eDOS, the presence of V_{Sn} defect makes the material more p-type as the Fermi level moves further deep inside the valence band; this correlates well with our experimental results of increase in carrier concentration with radiation dosage. The presence of gap states induces energy filtering effect which distorts the phonon transport without disturbing the electron mobility in the host. On the contrary, presence of V_{Se} defect increases the bandgap to 0.6 eV which implies that the charged Se vacancy defect acts as a deep donor and compensates the hole carrier concentration to form n-type conduction (figure 3f), which is not observed experimentally. For better interpretation of the intrinsic defect induced alteration in the theoretical electronic density of states, we also calculated the defect formation energies of the native defects in SnSe system as shown in figure 4b and 4c. For the defect formation enthalpies of various intrinsic defects, we used the following equation:

$$E_{form}^{Defect,q}(\Delta E_F) = E_{Total}^{Defective,q} - E_{Total}^{host} + \sum_i n_i \mu_i + q(E_{VBM}^{Host} + \Delta E_F)$$

where $E_{Total}^{Defective,q}$ and E_{Total}^{host} are the total energies of defective structure and defect-free supercell structure obtained from the VASP DFT calculations, respectively, n_i is the total number of atoms in the supercell, μ_i is the atomic chemical potential of the defective element, q is the charge state of the defect and E_F is the Fermi level, respectively. Figure 4b and 4c show the defect formation energies of intrinsic point defects under different charge states in Sn-rich and Se-rich conditions. In our case of SnSe crystal, the possibility of intrinsic point defects is Sn vacancy(V_{Sn}), Se vacancy(V_{Se}), interstitial defects of Sn (Sn_i) and Se (Se_i), substitutional defects of Sn(Sn_{Se}) and Se(Sn_{Se}) respectively. Under Sn-rich and Se-rich conditions, the predominant vacancy defects V_{Sn}

and V_{Se} exhibit relatively lower formation energies than other defects in their neutrally charged ($q=0$) state. As observed under Sn-rich condition, the formation energies of Se vacancy, interstitial Sn and substitutional Sn_{Se} defects exhibits lower formation energies. On the other hand, the defects Sn vacancy, Se interstitial and Se substitutional Se_{Sn} exhibit lower formation energies under Se-rich condition. Under both conditions, V_{Sn} ($q=-2$) demonstrates the lowest formation energy of all the prevailing intrinsic defects, acting as an ultra-shallow acceptor. However, V_{Se} ($q=+1$) defect also exhibits relatively lower formation energy and behaves as a deep donor defect, V_{Sn} dominates V_{Se} suppressing the effect of n-type conduction³⁴. Thus the formation V_{Sn} defect is more dominating than other intrinsic defects and contributes to the p-type nature in the SnSe host.

Further, to understand the effect of intrinsic defects on phonon transport, a detailed study on the lattice dynamics of SnSe under defect rich conditions were performed as illustrated in Supplementary data S3. For the defect-free SnSe lattice structure, the phonon states lie sparsely occupied between 0.5-2.5 THz range. Under Sn vacancy defect rich condition, the defects tend to introduce large number of phonon states between 1-5 THz range which is also abruptly seen in the phonon density of states plot. The generation of Sn vacancy defect-related bands in the phonon dispersion roots to enhanced phonon-phonon scattering and phonon-defect scattering phenomenon resulting in lower lattice thermal conductivity through lattice anharmonicity⁴⁹. Whereas, in the case of Se vacancy rich condition, the defect generated phonon states are split between lower and higher frequency ranges, which also supports inducing additional lattice anharmonicity for phonon scattering. Collectively, the comparison of phonon dispersion and phonon density of states under defect-rich conditions introduces additional phonon states leading to a more significant reduction in phonon mean free path and thus lowering phonon lifetime in the system^{16,50}. The Raman spectroscopy analysis shows three strong peaks at 106.2 cm^{-1} , 125.3 cm^{-1} and 148 cm^{-1} , which relate with B_{3g} and two A_g Raman modes, respectively⁵¹. The relative intensities of these Raman modes decrease with an increase in radiation dose rate; the A_g mode (125.3 cm^{-1}) shows an evident broadening of the existence of lattice anharmonicity generated through the increasing lattice defect concentration⁵¹. With the increase in the defect concentration, the A_g peak at 180 cm^{-1} shows an apparent increase in intensity. Raman intensity and peak broadening effect observed can be related to lattice anharmonicity and lattice dislocations which play a significant role in phonon scattering. Raman mapping images shown in figure 5b demonstrate a significant decreasing trend of Raman peak intensities with the increasing alpha irradiation dosage.

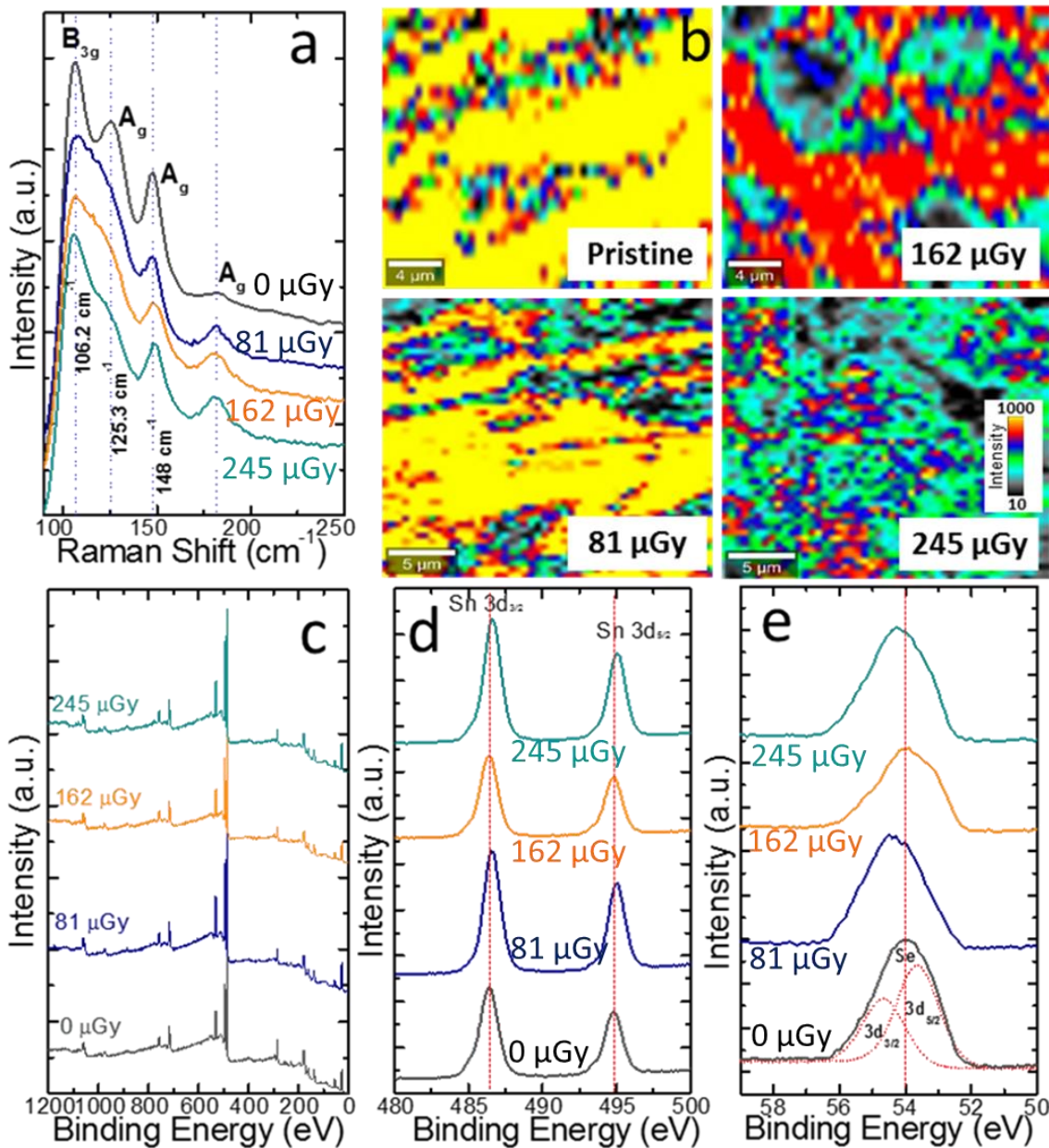


Figure 5 (a) Raman spectra of SnSe showing peak shift and broadening under different radiation dosage (b) Raman mapping exhibiting the change in peak intensity with respect to the irradiation dosage (c) shows the full survey scan of the SnSe sample under different radiation dosage (d) and (e) explains the high-resolution scan for Sn 3d and Se 3d states respectively.

To precisely determine the material atomic composition and the chemical states of the element present, X-ray photoelectron spectroscopy is used. The presence of defects in the material alter the bonding energies or create a new peak with different bonding energy or peak shifting. Comparing the relative elemental percentage, peak binding energy position and peak intensity, a detailed

analysis of the existing defect is obtained⁵². Figure 5c shows the full survey scan for the pristine SnSe and the radiation exposed sample with varying dosage levels, which indicates the presence of Sn 3d and Se 3d energy states without impurities other than carbon and oxygen states. For detailed information of peak position and bonding energy changes the high-resolution scan for Sn 3d and Se 3d states were performed. The high-resolution scan for Sn shows two peaks of Sn 3d_{3/2} and Sn 3d_{5/2} at 494.79 eV and 486.4 eV, respectively. The peak at the binding energy of 486.4 eV can be rationalized into Sn⁴⁺ and Sn²⁺ at 486.4 eV and 485.5 eV, of which Sn⁴⁺ is bonded to Se²⁻ and Sn²⁺ is bonded to Se²⁻ respectively. As seen in figure 5d and 5e, the peaks of Sn 3d_{3/2} and Sn 3d_{5/2} show a clear peak shift with increasing radiation dosage, indicating the formation of Sn related intrinsic defects in the material⁵³. High-resolution scan of Se reveals the presence peak at 53.95 eV which can be rationalized into Se 3d_{3/2} and Se 3d_{5/2} at 54.66 eV and 53.65 eV respectively⁵⁴. Similar to that of Sn 3d peaks, the Se 3d also shows a redshift with increasing radiation dosage. Thus from XPS analysis, it is clear that the co-existence of intrinsic defects in the material and their defect densities are enhanced with the change in radiation dosage.

Table 1: Electronic transport properties with respect to alpha irradiation dosage at room temperature.

Irradiation Dosage (μGy)	Carrier Concentration ($\times 10^{18} \text{ cm}^{-3}$)	Seebeck Coefficient ($\mu\text{V/K}$)	Electrical Conductivity (S/cm)	Fermi level E_f (eV)	Effective Mass	Effective Density of States (states/cm ³)
0	0.72	303.65	7	0.03598	0.0695	4.61E+17
81	1.53	308	10	0.03855	0.283745	3.80E+18
162	3.34	294	11.5	0.03341	0.38471	6.01E+18
245	17	297.7	12	0.03341	1.047202	2.70E+19

Temperature-dependent hall measurements were performed to investigate the effect of the radiation dosage induced charged Sn vacancies on the electrical transport properties of the material. At room temperature, the hole concentration of the pristine and radiation-exposed SnSe samples demonstrates increasing from the order of 10^{17} to 10^{19} cm^{-3} , as shown in figure 2e⁴⁵. At 300K, the sample with an applied irradiation dosage of 245 μGy reaches a higher hole concentration of $1.7 \times 10^{19} \text{ cm}^{-3}$ compared to the pristine polycrystalline SnSe with $7.2 \times 10^{17} \text{ cm}^{-3}$, this significant enhancement is only possible through the introduction of charged Sn vacancy defects in the material⁵⁵. This change in the carrier concentration induced by the defects leads to a larger variation in effective mass, as shown in Table 1.

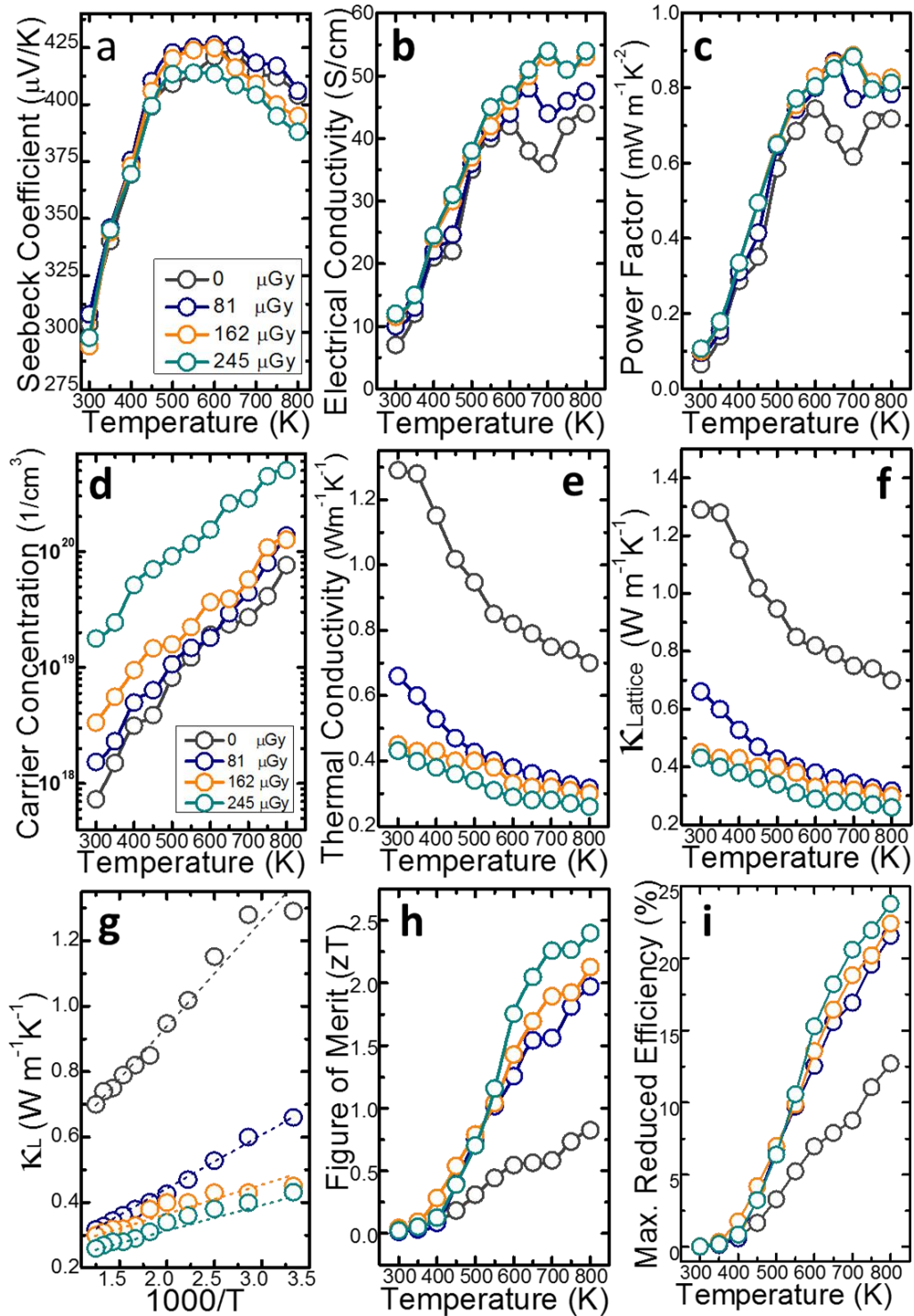


Figure 6 Temperature-dependent (a) Seebeck coefficient, (b) Electrical conductivity (c) Power Factor (d) carrier concentration (e) total thermal conductivity (f) demonstrates the effects of intrinsic defects induced by the respective radiation dosages on lattice thermal conductivity of SnSe (g) κ_L as a function of $1000/T$ (h) shows the comparison of their achieved figure of merit (zT) (i) Maximum reduced efficiency of the thermoelectric power conversion with temperature.

In SnSe, under the Sn vacancy rich condition, V_{Sn} defects are considered major acceptors, leading to massive enhancement in their electrical conductivity. As the carrier concentration and the hole mobility are the major parameters governing the thermoelectric performance, we have demonstrated their temperature dependency in the material, as shown in figure 6d. The carrier concentration for all the irradiation doses increases with temperature resembling the thermal activation of the induced charge carriers. In contrast, the mobility shows a decreasing trend owing to the carrier scattering with temperature. The carrier scattering mechanism can be explained by the power-law $\mu \sim T^{-r}$, where r is the carrier scattering parameter. Supplementary data S4(b) shows the relation between $\mu \sim T^{-1.5}$, which purely demonstrates the carrier scattering is dominated by acoustic phonon scattering^{45,53}. Carrier mobility drops as the irradiation dosage increases due to induced crystal lattice defects in the SnSe, which drastically affects the charge mobility. The combined effect of the carrier density and mobility with the temperature typically activates the semiconducting behaviour achieved by thermal activation of charge carriers, enhancing the electrical conductivity of the material.

Thermoelectric performance of SnSe based on their anisotropy along different axes in previous literature^[45] proves that dominated along the in-plane direction (\perp direction) compared to the out-of-plane direction (\parallel direction). Our study also experienced the same effect, which is the reason for presenting only the results along the in-plane (\perp direction) in this work. Temperature-dependent Seebeck coefficient (S) measurement for the pristine and alpha irradiation-exposed samples with dosage level of 81 μGy , 162 μGy and 245 μGy , respectively, are presented in figure 6a. Seebeck coefficient values show increasing trends with maximum values at 625K and the positive values of S signify the p-type nature. The fall of S values at $T > 650$ K is due to minority carrier excitation and leads to bipolar conduction. The radiation-exposed samples demonstrate slight decreasing drifts in Seebeck coefficient values due to Sn vacancies' increase in hole density. However, the radiated sample with 81 μGy dosages shows an increased Seebeck coefficient of 430 $\mu\text{V/K}$ compared to pristine SnSe of 415 $\mu\text{V/K}$ at 600 K. The temperature-dependent variation in electrical conductivity (σ) of SnSe is shown in figure 6b. The electrical conductivity of the irradiated samples exhibits increasing trends with the radiation dosage compared to pristine SnSe. Initially, between 300 – 500K, the temperature-dependent semiconducting transport performance occurs as the electrons (minority carriers) are thermally excited from the valence band to the defect

acceptor bands. After the saturation of the defect acceptor band, the electrical conductivity of SnSe shows metallic nature owing to phonon scattering up to 670 K. With further increase in temperature, the σ shows a fall and rise nature because of the phase transition from *Pnma* to *Cmcm* after 700 K⁵⁶. As observed, the electrical conductivity of radiation-exposed SnSe samples tends to increase with increasing Sn²⁺ vacancies and the sample with a radiation dose of 245 μ Gy shows the highest σ of 55 S/cm at 700 K. Following the rise in electrical conductivity due to Sn vacancies, the power factor ($S^2\sigma$) shows a significant increase compared to pristine SnSe samples. The maximum power factor of 0.9 mW m⁻¹K⁻² is achieved for 162 μ Gy and 245 μ Gy samples and it is the largest power factor ever reported for SnSe. The effect of the intrinsic defects on the thermal conductivity of SnSe has been investigated in detail, as shown in Figure 6e and 6f. The total thermal conductivity (K_{Total}) of pristine SnSe and defect induced SnSe samples shows a common decreasing trend as a function of temperature. The intrinsic defect generated through the radiation dosages collectively diminished the lifetime and mean free path of phonons and leading to an ultralow thermal conductivity compared to other reports on doped SnSe. To effectively investigate the variation in electronic ($K_{Electronic}$) and lattice ($K_{Lattice}$) thermal conductivity, using Wiedemann-Franz law ($K_{Electronic} = L\sigma T$), the $K_{Lattice}$ is deduced from the relation $K_{Lattice} = K_{Total} - K_{Electronic}$ ⁵⁷. The Lorenz number is calculated using the Fermi energy with the one-band model by considering only the acoustic phonon scattering as shown in supplementary data S4(d) and the electronic thermal conductivity increases with electrical conductivity. However, the lattice thermal conductivity shown in figure 6f demonstrates the dominating influence of phonon dynamics over the electronic part of thermal conductivity. The synergistic impact of the induced Sn vacancy and other intrinsic defects induced by the radiation is observed through their respective suppressed lattice thermal conductivity values compared to the pristine SnSe. This massive reduction in the lattice thermal conductivity of the irradiated samples arises from the enhanced phonon scattering by the presence of Sn vacancies and Se vacancies in the lattice^{41,58}. The lowest value of 0.24 W m⁻¹K⁻¹ at 800 K is reached for the sample with a radiation dosage of 245 μ Gy. Figure 6g exhibits the trend of $K_{Lattice}$ vs 1000/T, which shows the linear relationship signifying the phonon scattering is purely dominated by the phonon-umklapp scattering. This linear trend signifies the strong anharmonicity induced by the irradiation dosages achieving ultralow lattice thermal conductivity. Our phonon dispersion calculation under Sn and Se vacancy rich conditions very well support the obtained

ultra-low lattice thermal conductivity values through the defect dominated lattice anharmonicity. As a result of the enhanced power factor and suppressed Lattice thermal conductivity, the zT increases to a maximum value of 2.4 at 800 K in our p-type polycrystalline SnSe as shown in Figure 6i. This enhancement is reproducible for several batches of materials synthesized at various time and repeated measurements as shown in supplementary data S5. From the calculated zT values, it is witnessed that optimization of intrinsic defect engineering in SnSe plays a major role in enhancing the thermoelectric performance of the material. The calculated thermoelectric power conversion efficiency is shown in figure 6m, which reaches the peak efficiency of 25% compared with the pristine defect-free SnSe sample demonstrating only 13% efficiency. These power conversion efficiency value is comparable to any other renewable energy source.

4. Conclusion

Through a simple and cost-effective mechanical alloying method, we have successfully synthesized a polycrystalline SnSe and thereby engineering their intrinsic defects through controlled alpha irradiation eventually, high thermoelectric performance in SnSe is achieved. From the theoretical calculation of defect formation energies and electronic density of states, the mechanism of inducing high Sn vacancies is the reason for its native p-type conduction and ultra-low thermal conductivity. Further, the calculated phonon dispersion curves prove that the presence of Sn and Se vacancy defects introduces additional phonon-defect scattering in the system. Synergistically, the presence of Sn vacancies significantly suppressed the lattice thermal conductivity due to the enhanced phonon-defect scattering produced by the lattice anharmonicity. Collectively, through the controlled dosage of alpha-radiation, we have optimized the intrinsic defect level in the SnSe which lead to enhanced thermoelectric performance with zT value of 2.4 and ultralow lattice thermal conductivity of 0.24 W/m/K at 800 K. Finally, by this strategy of optimizing the intrinsic defects in the SnSe thermoelectric materials we have achieved the highest thermoelectric power conversion efficiency of 25% in SnSe, which is comparable to any other renewable power sources.

Supporting Information

The Supporting information data is available for: TRIM Simulation, defect-free pristine SnSe TEM, Theoretical calculation for phonon scattering, Temperature dependent carrier mobility,

repeatability data for thermoelectric parameters and anisotropy dependent thermoelectric parameters of SnSe samples.

Acknowledgement

We acknowledge grants from the Research Grants Council of Hong Kong Special Administrative Region Project no: T42-103/16N and Environmental & Conservation Fund (ECF) project number 44/2014. We thank Prof. Peter. K. N. Yu for providing the Alpha particle irradiation source for the experiment.

Conflict of Interest

The authors declare no conflict of interest.

Author Contribution

Vaithinathan Karthikeyan: Designed and performed the experiment, drafted the manuscript; **Saw Lin Oo:** performed the alpha irradiation experiment; **James Utama Surjadi, Xiaocui Li and Yang Lu:** helped in performing the FESEM and TEM measurement and analysis; **Vaskuri C. S. Theja:** Supported in Raman mapping measurement and analysis; **Venkataramanan Kannan and Siu Chuen Lau:** Interpreted and validated the thermoelectric measurement results; **Kwok-Ho Lam** performed thermal conductivity measurements; **Vellaisamy A. L. Roy:** Supervised the project.

Reference

- (1) Aswal, D. K.; Basu, R.; Singh, A. Key Issues in Development of Thermoelectric Power Generators: High Figure-of-Merit Materials and Their Highly Conducting Interfaces with Metallic Interconnects. *Energy Conversion and Management*. **2016**, *114*, 50.
- (2) Kim, H. S.; Liu, W.; Ren, Z. The Bridge between the Materials and Devices of Thermoelectric Power Generators. *Energy Environ. Sci.* **2017**, *10* (1), 69–85.
- (3) Shi, X.; Chen, L.; Uher, C. Recent Advances in High-Performance Bulk Thermoelectric Materials. *Int. Mater. Rev.* **2016**, *61* (6), 379–415.
- (4) Dresselhaus, M. S.; Dresselhaus, G.; Fleurial, J.-P.; Caillat, T. Recent Developments in Thermoelectric Materials. *Int. Mater. Rev.* **2003**, *48* (1), 45–66.

- (5) Freer, R.; Powell, A. V. Realising the Potential of Thermoelectric Technology: A Roadmap. *J. Mater. Chem. C* **2020**, *8* (2), 441–463.
- (6) Tan, G.; Zhao, L. D.; Kanatzidis, M. G. Rationally Designing High-Performance Bulk Thermoelectric Materials. *Chemical Reviews*. **2016**, *116*, 12123–12149.
- (7) Wang, H.; Pei, Y.; LaLonde, A. D.; Snyder, G. J. Weak Electron–Phonon Coupling Contributing to High Thermoelectric Performance in n-Type PbSe. *Proc. Natl. Acad. Sci.* **2012**, *109* (25), 9705 – 9709.
- (8) Pei, Y.; LaLonde, A. D.; Heinz, N. A.; Shi, X.; Iwanaga, S.; Wang, H.; Chen, L.; Snyder, G. J. Stabilizing the Optimal Carrier Concentration for High Thermoelectric Efficiency. *Adv. Mater.* **2011**, *23* (47), 5674–5678.
- (9) Tan, X. J.; Liu, G. Q.; Xu, J. T.; Shao, H. Z.; Jiang, J.; Jiang, H. C. Element-Selective Resonant State in M-Doped SnTe (M = Ga, In and Tl). *Phys. Chem. Chem. Phys.* **2016**, *18* (30), 20635–20639.
- (10) Hu, L.; Zhang, Y.; Wu, H.; Li, J.; Li, Y.; Mckenna, M.; He, J.; Liu, F.; Pennycook, S. J.; Zeng, X. Entropy Engineering of SnTe: Multi-Principal-Element Alloying Leading to Ultralow Lattice Thermal Conductivity and State-of-the-Art Thermoelectric Performance. *Adv. Energy Mater.* **2018**, *8* (29), 1802116.
- (11) Chen, Z.; Jian, Z.; Li, W.; Chang, Y.; Ge, B.; Hanus, R.; Yang, J.; Chen, Y.; Huang, M.; Snyder, G. J.; Pei, Y. Lattice Dislocations Enhancing Thermoelectric PbTe in Addition to Band Convergence. *Adv. Mater.* **2017**, *29* (23), 1–8.
- (12) Guo, Y.; Du, X.; Wang, Y.; Yuan, Z. Simultaneous Enhanced Performance of Electrical Conductivity and Seebeck Coefficient in Bi_{2–x}Sn_xS₃ by Solvothermal and Microwave Sintering. *J. Alloys Compd.* **2017**, *717*, 177–182.
- (13) Lee, M. H.; Byeon, D.-G.; Rhyee, J.-S.; Ryu, B. Defect Chemistry and Enhancement of Thermoelectric Performance in Ag-Doped Sn_{1+δ-x}Ag_xTe. *J. Mater. Chem. A* **2017**, *5* (5) 2235.
- (14) Thébaud, S.; Adessi, C.; Pailhès, S.; Bouzerar, G. Boosting the Power Factor with Resonant States: A Model Study. *Phys. Rev. B* **2017**, *96* (7), 1–7.

- (15) Viskadourakis, Z.; Athanasopoulos, G. I.; Kasotakis, E.; Giapintzakis, J. Effect of Microstructure on the Thermoelectric Performance of $\text{La}_{1-x}\text{Sr}_x\text{CoO}_3$. *J. Solid State Chem.* **2016**, *243*, 111–118.
- (16) Meng, X.; Liu, Z.; Cui, B.; Qin, D.; Geng, H.; Cai, W.; Fu, L.; He, J.; Ren, Z.; Sui, J. Grain Boundary Engineering for Achieving High Thermoelectric Performance in N-Type Skutterudites. *Adv. Energy Mater.* **2017**, *13*, 1602582.
- (17) Sun, Y.; Cheng, H.; Gao, S.; Liu, Q.; Sun, Z.; Xiao, C.; Wu, C.; Wei, S.; Xie, Y. Atomically Thick Bismuth Selenide Freestanding Single Layers Achieving Enhanced Thermoelectric Energy Harvesting. *J. Am. Chem. Soc.* **2012**, *134* (50), 20294–20297.
- (18) Deng, R.; Su, X.; Hao, S.; Zheng, Z.; Zhang, M.; Xie, H.; Liu, W.; Yan, Y.; Wolverton, C.; Uher, C.; Kanatzidis, M. G.; Tang, X. High Thermoelectric Performance in $\text{Bi}_{0.46}\text{Sb}_{1.54}\text{Te}_3$ Nanostructured with ZnTe. *Energy Environ. Sci.* **2018**, *11* (6), 1520–
- (19) Tang, Y.; Hanus, R.; Chen, S.-W.; Snyder, G. J. ARTICLE Solubility Design Leading to High Figure of Merit in Low-Cost Ce-CoSb₃ Skutterudites. **2015**, *6*, 7584.
- (20) Shin, W. H.; Roh, J. W.; Ryu, B.; Chang, H. J.; Kim, H. S.; Lee, S.; Seo, W. S.; Ahn, K. Enhancing Thermoelectric Performances of Bismuth Antimony Telluride via Synergistic Combination of Multiscale Structuring and Band Alignment by FeTe₂ Incorporation. *ACS Appl. Mater. Interfaces* **2018**, *10* (4), 3689–3698.
- (21) Zhao, L.-D.; Lo, S.-H.; Zhang, Y.; Sun, H.; Tan, G.; Uher, C.; Wolverton, C.; Dravid, V. P.; Kanatzidis, M. G. Ultralow Thermal Conductivity and High Thermoelectric Figure of Merit in SnSe Crystals. *Nature* **2014**, *508* (7496), 373–377.
- (22) Hong, J.; Delaire, O. Electronic Instability and Anharmonicity in SnSe. *Materials Today Physics* **2019**, *10*, 100093.
- (23) Li, C. W.; Hong, J.; May, A. F.; Bansal, D.; Chi, S.; Hong, T.; Ehlers, G.; Delaire, O. Orbitally Driven Giant Phonon Anharmonicity in SnSe. *Nat. Phys.* **2015**, *11* (12), 1063–1069.
- (24) Hong, M.; Lyv, W.; Li, M.; Xu, S.; Sun, Q.; Zou, J.; Chen, Z.-G. Rashba Effect Maximizes Thermoelectric Performance of GeTe Derivatives. *Joule* **2020**, *4* (9), 2030–

2043.

- (25) Sun, S.; Li, P.; Liang, S.; Yang, Z. Diversified Copper Sulfide (Cu_{2-x}S) Micro-/Nanostructures: A Comprehensive Review on Synthesis, Modifications and Applications. *Nanoscale* **2017**, *9* (32), 11357–11404.
- (26) Park, J. G.; Lee, Y. H. High Thermoelectric Performance of Bi-Te Alloy: Defect Engineering Strategy. *Curr. Appl. Phys.* **2016**, *16* (9), 1202–1215.
- (27) Acharya, S.; Pandey, J.; Soni, A. Soft Phonon Modes Driven Reduced Thermal Conductivity in Self-Compensated $\text{Sn}_{1.03}\text{Te}$ with Mn Doping. *Appl. Phys. Lett.* **2016**, *109* (13), 1–6..
- (28) Zhao, L. D.; Lo, S. H.; Zhang, Y.; Sun, H.; Tan, G.; Uher, C.; Wolverton, C.; Dravid, V. P.; Kanatzidis, M. G. Ultralow Thermal Conductivity and High Thermoelectric Figure of Merit in SnSe Crystals. *Nature* **2014**, *508* (7496), 373–377.
- (29) Liang, S.; Xu, J.; Noudem, J. G.; Wang, H.; Tan, X.; Liu, G.-Q.; Shao, H.; Yu, B.; Yue, S.; Jiang, J. Thermoelectric Properties of Textured Polycrystalline $\text{Na}_{0.03}\text{Sn}_{0.97}\text{Se}$ Enhanced by Hot Deformation. *J. Mater. Chem. A* **2018**, *6* (46), 23730–23735.
- (30) Xiao, Y.; Chang, C.; Pei, Y.; Wu, D.; Peng, K.; Zhou, X.; Gong, S.; He, J.; Zhang, Y.; Zeng, Z.; Zhao, L. D. Origin of Low Thermal Conductivity in SnSe. *Phys. Rev. B* **2016**, *94* (12), 5–10.
- (31) Zhao, L. D.; Chang, C.; Tan, G.; Kanatzidis, M. G. SnSe: A Remarkable New Thermoelectric Material. *Energy Environ. Sci.* **2016**, *9* (10), 3044–3060.
- (32) Duvjir, G.; Min, T.; Thi Ly, T.; Kim, T.; Duong, A.-T.; Cho, S.; Rhim, S. H.; Lee, J.; Kim, J. Origin of P-Type Characteristics in a SnSe Single Crystal. *Appl. Phys. Lett.* **2017**, *110* (26), 262106.
- (33) Ge, Z.-H.; Qiu, Y.; Chen, Y.-X.; Chong, X.; Feng, J.; Liu, Z.-K.; He, J. Multipoint Defect Synergy Realizing the Excellent Thermoelectric Performance of N-Type Polycrystalline SnSe via Re Doping. *Adv. Funct. Mater.* **2019**, *29* (28), 1902893.
- (34) Zhou, Y.; Li, W.; Wu, M.; Zhao, L. D.; He, J.; Wei, S. H.; Huang, L. Influence of Defects

- on the Thermoelectricity in SnSe: A Comprehensive Theoretical Study. *Phys. Rev. B* **2018**, *97* (24), 1–8.
- (35) Lee, Y. K.; Luo, Z.; Cho, S. P.; Kanatzidis, M. G.; Chung, I. Surface Oxide Removal for Polycrystalline SnSe Reveals Near-Single-Crystal Thermoelectric Performance. *Joule* **2019**, *3* (3), 719–731.
- (36) Zhao, Q.; Qin, B.; Wang, D.; Qiu, Y.; Zhao, L.-D. Realizing High Thermoelectric Performance in Polycrystalline SnSe via Silver Doping and Germanium Alloying. *ACS Appl. Energy Mater.* **2020**, *3* (3), 2049–2054.
- (37) M, S.; Amirthapandian, S.; Magudapathy, P.; Srivastava, S. K.; Asokan, K. Tuning of the Thermoelectric Properties of Bi₂Te₃ Nanorods Using Helium Ion Irradiation. *ACS Omega* **2018**, *3* (12), 18411–18419.
- (38) Suh, J.; Yu, K. M.; Fu, D.; Liu, X.; Yang, F.; Fan, J.; Smith, D. J.; Zhang, Y.-H.; Furdyna, J. K.; Dames, C.; Walukiewicz, W.; Wu, J. Simultaneous Enhancement of Electrical Conductivity and Thermopower of Bi₂Te₃ by Multifunctionality of Native Defects. *Adv. Mater.* **2015**, *27* (24), 3681–3686.
- (39) Goo, G.; Anoop, G.; Unithrattil, S.; Kim, W. S.; Lee, H. J.; Kim, H. Bin; Jung, M.-H.; Park, J.; Ko, H. C.; Jo, J. Y. Proton-Irradiation Effects on the Thermoelectric Properties of Flexible Bi₂Te₃/PEDOT:PSS Composite Films. *Adv. Electron. Mater.* **2019**, *5* (4), 1800786.
- (40) Dudarev, S. L.; Botton, G. A.; Savrasov, S. Y.; Humphreys, C. J.; Sutton, A. P. Electron-Energy-Loss Spectra and the Structural Stability of Nickel Oxide: An LSDA+U Study. *Phys. Rev. B* **1998**, *57* (3), 1505–1509.
- (41) Karthikeyan, V.; Arava, C. M.; Hlaing, M. Z.; Chen, B.; Chan, C. H.; Lam, K.-H.; Roy, V. A. L. Dislocation-Induced Ultra-Low Lattice Thermal Conductivity in Rare Earth Doped β -Zn₄Sb₃. *Scr. Mater.* **2020**, *174*, 95–101.
- (42) Zhang, B.; Peng, K.; Li, A.; Zhou, X.; Chen, Y.; Deng, Q.; Han, X. The Chemistry and Structural Thermal Stability of Hole-Doped Single Crystalline SnSe. *J. Alloys Compd.* **2016**, *688*, 1088–1094.

- (43) Choi, G.; Bahk, Y. M.; Kang, T.; Lee, Y.; Son, B. H.; Ahn, Y. H.; Seo, M.; Kim, D. S. Terahertz Nanoprobng of Semiconductor Surface Dynamics. *Nano Lett.* **2017**, *17* (10), 6397–6401.
- (44) Ulbricht, R.; Hendry, E.; Shan, J.; Heinz, T. F.; Bonn, M. Carrier Dynamics in Semiconductors Studied with Time-Resolved Terahertz Spectroscopy. *Rev. Mod. Phys.* **2011**, *83* (2), 543–586.
- (45) Shi, X.; Chen, Z.-G.; Liu, W.; Yang, L.; Hong, M.; Moshwan, R.; Huang, L.; Zou, J. Achieving High Figure of Merit in P-Type Polycrystalline Sn_{0.98}Se via Self-Doping and Anisotropy-Strengthening. *Energy Storage Mater.* **2018**, *10*, 130–138.
- (46) Huang, Y.; Wang, C.; Chen, X.; Zhou, D.; Du, J.; Wang, S.; Ning, L. First-Principles Study on Intrinsic Defects of SnSe. *RSC Adv.* **2017**, *7* (44), 27612–27618.
- (47) Wang, Z.; Fan, C.; Shen, Z.; Hua, C.; Hu, Q.; Sheng, F.; Lu, Y.; Fang, H.; Qiu, Z.; Lu, J.; Liu, Z.; Liu, W.; Huang, Y.; Xu, Z. A.; Shen, D. W.; Zheng, Y. Defects Controlled Hole Doping and Multivalley Transport in SnSe Single Crystals. *Nat. Commun.* **2018**, *9* (1), 47.
- (48) Karthikeyan, V.; Li, T.; Medasani, B.; Luo, C.; Shi, D.; Wong, J. C. K.; Lam, K.-H.; Ling, F. C. C.; Roy, V. A. L. Defect and Dopant Mediated Thermoelectric Power Factor Tuning in β -Zn₄Sb₃. *Adv. Electron. Mater.* **2020**, *6*, 1901284.
- (49) Skelton, J. M.; Burton, L. A.; Parker, S. C.; Walsh, A.; Kim, C. E.; Soon, A.; Buckeridge, J.; Sokol, A. A.; Catlow, C. R. A.; Togo, A.; Tanaka, I. Anharmonicity in the High-Temperature *Cmcm* Phase of SnSe: Soft Modes and Three-Phonon Interactions. *Phys. Rev. Lett.* **2016**, *117* (7), 1–6.
- (50) Kim, S. Il; Lee, K. H.; Mun, H. A.; Kim, H. S.; Hwang, S. W.; Roh, J. W.; Yang, D. J.; Shin, W. H.; Li, X. S.; Lee, Y. H.; Snyder, G. J.; Kim, S. W. Dense Dislocation Arrays Embedded in Grain Boundaries for High-Performance Bulk Thermoelectrics. *Science* **2015**, *348* (6230), 109 – 114.
- (51) Li, X. Z.; Xia, J.; Wang, L.; Gu, Y. Y.; Cheng, H. Q.; Meng, X. M. Layered SnSe Nano-Plates with Excellent in-Plane Anisotropic Properties of Raman Spectrum and Photo-Response. *Nanoscale* **2017**, *9* (38), 14558–14564.

- (52) Xiong, J.; Di, J.; Xia, J.; Zhu, W.; Li, H. Surface Defect Engineering in 2D Nanomaterials for Photocatalysis. *Adv. Funct. Mater.* **2018**, *28* (39), 1–19.
- (53) Shi, X.-L.; Zheng, K.; Liu, W.-D.; Wang, Y.; Yang, Y.-Z.; Chen, Z.-G.; Zou, J. Realizing High Thermoelectric Performance in N-Type Highly Distorted Sb-Doped SnSe Microplates via Tuning High Electron Concentration and Inducing Intensive Crystal Defects. *Adv. Energy Mater.* **2018**, *8* (21), 1800775.
- (54) Heo, S. H.; Jo, S.; Kim, H. S.; Choi, G.; Song, J. Y.; Kang, J. Y.; Park, N. J.; Ban, H. W.; Kim, F.; Jeong, H.; Jung, J.; Jang, J.; Lee, W. B.; Shin, H.; Son, J. S. Composition Change-Driven Texturing and Doping in Solution-Processed SnSe Thermoelectric Thin Films. *Nat. Commun.* **2019**, *10* (1), 864.
- (55) Chandra, S.; Biswas, K. Realization of High Thermoelectric Figure of Merit in Solution Synthesized 2D SnSe Nanoplates via Ge Alloying. *J. Am. Chem. Soc.* **2019**, *141* (15), 6141–6145.
- (56) Wei, W.; Chang, C.; Yang, T.; Liu, J.; Tang, H.; Zhang, J.; Li, Y.; Xu, F.; Zhang, Z.; Li, J. F.; Tang, G. Achieving High Thermoelectric Figure of Merit in Polycrystalline SnSe via Introducing Sn Vacancies. *J. Am. Chem. Soc.* **2018**, *140* (1), 499–505.
- (57) Kim, H. S.; Gibbs, Z. M.; Tang, Y.; Wang, H.; Snyder, G. J. Characterization of Lorenz Number with Seebeck Coefficient Measurement. *APL Mater.* **2015**, *3* (4), 041506.
- (58) Chen, Z.; Ge, B.; Li, W.; Lin, S.; Shen, J.; Chang, Y.; Hanus, R.; Snyder, G. J.; Pei, Y. Vacancy-Induced Dislocations within Grains for High-Performance PbSe Thermoelectrics. *Nat. Commun.* **2017**, *8*, 13828.

Table of Content (TOC) Figure

